Research Article | Vol. 24, No. 16 | 8 Aug 2016 | OPTICS EXPRESS 18024

Optics EXPRESS

High efficiency near diffraction-limited mid-infrared flat lenses based on metasurface reflectarrays

SHUYAN ZHANG,[1,8] MYOUNG-HWAN KIM,[2,3,8] FRANCESCO AIETA,[4] ALAN SHE,[1] TOBIAS MANSURIPUR,[5] ILAN GABAY,[1] MOHAMMADREZA KHORASANINEJAD,[1] DAVID ROUSSO,[1,6] XIAOJUN WANG,[7] MARIANO TROCCOLI,[7] NANFANG YU,[2] AND FEDERICO CAPASSO[1,*]

[1]*John A. Paulson School of Engineering and Applied Sciences, Harvard University, 9 Oxford Street, Cambridge, MA 02138, USA*
[2]*Department of Applied Physics & Applied Mathematics, Columbia University, 500 West 120th St, New York, NY 10027, USA*
[3]*Department of Physics, The University of Texas Rio Grande Valley, Brownsville, TX 78520, USA*
[4]*LEIA 3D, Menlo Park CA 94025, USA*
[5]*Department of Physics, Harvard University, 17 Oxford Street, Cambridge, MA 02138, USA*
[6]*University of Waterloo, Waterloo, ON N2L 3G1, Canada*
[7]*AdTech Optics, Inc., 18007 Courtney Court, City of Industry, CA 91748, USA*
[8]*These authors contributed equally.*
**capasso@seas.harvard.edu*

Abstract: We report the first demonstration of a mid-IR reflection-based flat lens with high efficiency and near diffraction-limited focusing. Focusing efficiency as high as 80%, in good agreement with simulations (83%), has been achieved at 45° incidence angle at $\lambda = 4.6$ μm. The off-axis geometry considerably simplifies the optical arrangement compared to the common geometry of normal incidence in reflection mode which requires beam splitters. Simulations show that the effects of incidence angle are small compared to parabolic mirrors with the same NA. The use of single-step photolithography allows large scale fabrication. Such a device is important in the development of compact telescopes, microscopes, and spectroscopic designs.

OCIS codes: (260.3060) Infrared; (220.3630) Lenses; (120.5060) Phase modulation.

References and links

1. A. Schliesser, N. Picque, and T. W. Hansch, "Mid-infrared frequency combs," Nat. Photonics **6**(7), 440–449 (2012).
2. R. Soref, "Mid-infrared photonics in silicon and germanium," Nat. Photonics **4**(8), 495–497 (2010).
3. Edmund Optics, "The correct material for infrared (IR) applications," *http://www.edmundoptics.com/resources/application-notes/optics/the-correct-material-for-infrared-applications/*.
4. N. Yu, P. Genevet, F. Aieta, M. A. Kats, R. Blanchard, G. Aoust, J. P. Tetienne, Z. Gaburro, and F. Capasso, "Flat optics: controlling wavefronts with optical antenna metasurfaces," IEEE J. Sel. Top. Quantum Electron. **19**(3), 4700423 (2013).
5. N. Yu and F. Capasso, "Flat optics with designer metasurfaces," Nat. Mater. **13**(2), 139–150 (2014).
6. N. M. Estakhri and A. Alù, "Recent progress in gradient metasurfaces," J. Opt. Soc. Am. B **33**(2), 71–80 (2016).
7. F. Aieta, P. Genevet, M. A. Kats, N. Yu, R. Blanchard, Z. Gaburro, and F. Capasso, "Aberration-free ultrathin flat lenses and axicons at telecom wavelengths based on plasmonic metasurfaces," Nano Lett. **12**(9), 4932–4936 (2012).
8. A. Arbabi, R. M. Briggs, Y. Horie, M. Bagheri, and A. Faraon, "Efficient dielectric metasurface collimating lenses for mid-infrared quantum cascade lasers," Opt. Express **23**(26), 33310–33317 (2015).
9. A. Arbabi, Y. Horie, A. J. Ball, M. Bagheri, and A. Faraon, "Subwavelength-thick lenses with high numerical apertures and large efficiency based on high-contrast transmitarrays," Nat. Commun. **6**, 7069 (2015).
10. D. Hu, X. Wang, S. Feng, J. Ye, W. Sun, Q. Kan, P. J. Klar, and Y. Zhang, "Ultrathin terahertz planar elements," Adv. Opt. Mat. **1**(2), 186–191 (2013).

#263620 http://dx.doi.org/10.1364/OE.24.018024
Journal © 2016 Received 20 Apr 2016; revised 20 Jul 2016; accepted 23 Jul 2016; published 29 Jul 2016

Optics EXPRESS

11. M. Khorasaninejad, W. T. Chen, R. C. Devlin, J. Oh, A. Y. Zhu, and F. Capasso, "Metalenses at visible wavelengths: Diffraction-limited focusing and subwavelength resolution imaging," Science **352**(6290), 1190–1194 (2016).
12. A. B. Klemm, D. Stellinga, E. R. Martins, L. Lewis, G. Huyet, L. O'Faolain, and T. F. Krauss, "Experimental high numerical aperture focusing with high contrast gratings," Opt. Lett. **38**(17), 3410–3413 (2013).
13. C. Saeidi and D. Weide, "Wideband plasmonic focusing metasurfaces," Appl. Phys. Lett. **105**(5), 053107 (2014).
14. N. Yu, F. Aieta, P. Genevet, M. A. Kats, Z. Gaburro, and F. Capasso, "A broadband, background-free quarter-wave plate based on plasmonic metasurfaces," Nano Lett. **12**(12), 6328–6333 (2012).
15. N. Yu, P. Genevet, M. A. Kats, F. Aieta, J.-P. Tetienne, F. Capasso, and Z. Gaburro, "Light propagation with phase discontinuities: generalized laws of reflection and refraction," Science **334**(6054), 333–337 (2011).
16. Y. C. Cheng, S. Kicas, J. Trull, M. Peckus, C. Cojocaru, R. Vilaseca, R. Drazdys, and K. Staliunas, "Flat focusing mirror," Sci. Rep. **4**, 6326 (2014).
17. D. Fattal, J. Li, Z. Peng, M. Fiorentino, and R. G. Beausoleil, "Flat dielectric grating reflectors with focusing abilities," Nat. Photonics **4**(7), 466–470 (2010).
18. A. Pors, M. G. Nielsen, R. L. Eriksen, and S. I. Bozhevolnyi, "Broadband focusing flat mirrors based on plasmonic gradient metasurfaces," Nano Lett. **13**(2), 829–834 (2013).
19. R. Lu, "Infrared microscopy applications" (2013), *http://www.gia.edu/gia-news-research-Infrared-Microscopy-Applications*.
20. J. M. Chalmers and P. R. Griffiths, "Vibrational spectroscopy: sampling techniques and fiber-optic probes," in *Applications of Vibrational Spectroscopy in Food Science*, E. Li-Chan, J. M. Chalmers, and P. R. Griffiths, eds. (Wiley, November 2010), pp. 67–68.
21. A. T. Tokunaga, T. Bond, J. Elias, M. Chun, M. Richter, M. Liang, J. Lacy, L. Daggert, E. Tollestrup, M. Ressler, D. Warren, S. Fisher, and J. Carr, "Design tradeoffs for a high spectral resolution mid-infrared echelle spectrograph on the Thirty-Meter Telescope," Proc. SPIE **6269**, 62693Y (2006).
22. S. Sun, Q. He, S. Xiao, Q. Xu, X. Li, and L. Zhou, "Gradient-index meta-surfaces as a bridge linking propagating waves and surface waves," Nat. Mater. **11**(5), 426–431 (2012).
23. S. Sun, K.-Y. Yang, C.-M. Wang, T.-K. Juan, W. T. Chen, C. Y. Liao, Q. He, S. Xiao, W.-T. Kung, G.-Y. Guo, L. Zhou, and D. P. Tsai, "High-efficiency broadband anomalous reflection by gradient meta-surfaces," Nano Lett. **12**(12), 6223–6229 (2012).
24. Lumerical Solutions, "Far field from periodic structures," *https://kb.lumerical.com/en/solvers_grating_projections_far_field.html*.
25. R. O'Connell, "Telescope optical design," in *ASTR 511: Astronomical Techniques*. Department of Astronomy, University of Virginia.
26. A. Epstein and G. V. Eleftheriades, "Huygens' metasurfaces via the equivalence principle: design and applications," J. Opt. Soc. Am. B **33**(2), A31–A50 (2016).
27. V. Asadchy, M. Albooyeh, S. Tcvetkova, Y. Ra'di, and S. A. Tretyakov, "Metasurfaces for perfect and full control of refraction and reflection," arXiv: 1603.07186 (2016).
28. F. Aieta, P. Genevet, M. Kats, and F. Capasso, "Aberrations of flat lenses and aplanatic metasurfaces," Opt. Express **21**(25), 31530–31539 (2013).
29. P. Wang, N. Mohammad, and R. Menon, "Chromatic-aberration-corrected diffractive lenses for ultra-broadband focusing," Sci. Rep. **6**, 21545 (2016).
30. Y. Li, X. Li, M. Pu, Z. Zhao, X. Ma, Y. Wang, and X. Luo, "Achromatic flat optical components via compensation between structure and material dispersions," Sci. Rep. **6**, 19885 (2016).
31. E. Arbabi, A. Arbabi, S. M. Kamali, Y. Horie, and A. Faraon, "Multiwavelength polarization insensitive lenses based on dielectric metasurfaces with meta-molecules," arXiv:1601.05847, 1–12 (2016).
32. M. Khorasaninejad, F. Aieta, P. Kanhaiya, M. A. Kats, P. Genevet, D. Rousso, and F. Capasso, "Achromatic metasurface lens at telecommunication wavelengths," Nano Lett. **15**(8), 5358–5362 (2015).
33. J. Cheng and H. Mosallaei, "Truly achromatic optical metasurfaces: a filter circuit theory-based design," J. Opt. Soc. Am. B **32**(10), 2115–2121 (2015).
34. F. Aieta, M. A. Kats, P. Genevet, and F. Capasso, " Multiwavelength achromatic metasurfaces by dispersive phase compensation," Science **347**(6228), 1342–1345 (2015).

1. Introduction

The interest in the applications of mid-infrared (IR) light has recently increased in many areas, such as trace-gas detection, biological and medical sensing, and environmental monitoring [1, 2]. Over the last decade, there has been major progress in the development of new IR sources and detectors. However, a limiting factor in the development of mid-wave and long-wave IR optics is the lack of suitable materials that are transparent, low cost, lightweight, and easy to machine [2–4].

A new class of optical components based on metasurfaces could be used to circumvent the limitations [5, 6]. These components control the wavefront of light using arrays of optical resonators with subwavelength dimensions, which are patterned on a surface to introduce a

Optics EXPRESS

desired spatial profile of optical phase. By tailoring the properties of each element of the array, one can spatially control the phase of the scattered light and consequently mold the wavefront. Based on this concept, various functionalities have since been reported in transmission mode covering a wide range of spectrum from the visible to the terahertz [4, 7–15]. In particular [8, 11], have reported focusing lenses with high efficiencies above 66% in the visible and in the mid-IR, respectively. In reflection mode, designs for focusing in the visible [16] and the near-IR [17, 18] have been reported. As far as we know, there has been no demonstration of a flat lens in reflection mode in the mid-IR and with high efficiency. Such a device would be ideal for compact catoptric and catadioptric systems such as Cassegrain telescopes, FT-IR microscopy and spectroscopic designs [19–21]. In particular, astronomers use reflecting telescopes because the lenses in large refractors are bulky, heavy and tend to bend and droop over time. Flat lens technology provides a solution of a lightweight, thin and compact design.

In this paper, we report the first high efficiency (80%) mid-IR (λ = 4.6 μm) reflection-based flat lens based on reflectarrays. A reflectarray metasurface is a multi-layered structure consisting of a planar array of antennas separated from a ground metallic plane by a dielectric spacer of subwavelength thickness [22, 23]. Experiments and simulations show that the focusing is near diffraction-limited. It is less sensitive to the change of incidence angle compared to its parabolic mirror counterpart in terms of reflection angle and focal length. The material and processing requirements of our lens are minimal, requiring only a flat reflective substrate and one photolithography step using conventional high-throughput photolithography steppers, which enables large-scale fabrication. Note that in [8], the mid-IR lens was fabricated using e-beam lithography, but we have successfully fabricated our device using photolithography, while tolerating larger fabrication errors than e-beam lithography. The experimental results agree well with the simulation ones considering these fabrication errors.

2. Lens design

As a proof of principle, we demonstrated a flat lens with the functionality of a cylindrical lens (one-dimensional focusing). A schematic of the flat lens is shown in Fig. 1(a): a collimated Gaussian beam arrives at the flat lens at an oblique incidence angle θ, and is focused at a length f in the direction normal to the lens surface. The reason for the oblique incidence is purely practical: by using the metasurface itself to spatially separate the incident and reflected beams, we avoid the need for a beam splitter to separate the two beams. This technique simplifies the experimental setup and eliminates the insertion loss introduced by a beam-splitter [12, 18], which improves weak signal detection.

In order to achieve the desired focusing for $\theta = 0°$, the phase profile of the wavefront as a function of position x along the metasurface lens must satisfy [13]:

$$\varphi_{focus}(x)=\frac{2\pi}{\lambda_0}\times\left(f-\sqrt{x^2+f^2}\right). \tag{1}$$

where λ_0 is the wavelength. There is no phase modulation along the y-direction, resulting in a focal line rather than a point. The oblique incident beam arrives with a linear phase gradient of its own, which we can cancel out using the metasurface by applying an additional phase profile:

$$\varphi_{linear}(x,\theta)=-\frac{2\pi}{\lambda_0}\times\left[x\times\sin(\theta)\right]. \tag{2}$$

Thus, we engineer the total phase shift φ of the lens to be

$$\varphi(x)=\varphi_{focus}(x)+\varphi_{linear}(x). \tag{3}$$

Optics EXPRESS

The total phase function was realized by subwavelength antennas of fixed center-to-center separation. The unit cell of the reflectarray is shown in Fig. 1(b). We take advantage of the interaction of the antenna with its mirror image in the ground plane: the near-field coupling between the antenna and its image results in a reflected field with a broad phase coverage without polarization conversion [7, 10]. At each center position x, the disc radius was chosen such that its phase response was closest to the calculated value $\varphi(x)$ (Appendix).

Using this method, we designed a flat lens for the parameters: θ = 45°, f = 80 mm, and W = 3.08 mm in both x- and y-directions. The numerical aperture (NA) of our lens is 0.02, which can be increased by decreasing the focal length or increasing the size of the lens itself [7, 18]. We fabricated the flat lens on a 6-inch fused silica wafer substrate. The deposition of the gold (Au) back reflector layer and discs was done by electron-beam evaporation. The silicon dioxide (SiO_2) dielectric spacer layer was deposited using plasma-enhanced chemical vapor deposition. The antenna patterns were fabricated using a stepper photolithography tool (GCA AS200 i-line stepper), which allows for large-scale fabrication. Figure 1(c) shows a scanning electron microscope image of a small section of the fabricated lens. Note that the 6-inch wafer substrate can accommodate over 160 such lenses with different focusing properties, such as focal lengths and reflection angles.

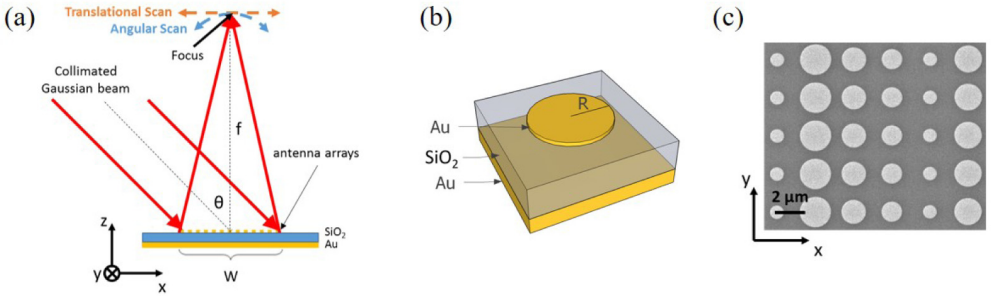

Fig. 1. (a) Geometry of the flat lens based on reflectarray antennas. W is the width of the lens. The focus is a narrow line in the y-direction which is characterized by angular and translational scans indicated by the blue and orange dashed lines, respectively. The drawing is not to scale. s (b) Schematic of the unit cell of the reflectarray lens: a 50 nm-thick gold disc is separated from a 200 nm-thick gold back reflector layer by a 400 nm-thick SiO_2 spacer. The size of the unit cell is 2.5 μm x 2.5 μm. (c) Scanning electron microscope image of a small section of the fabricated antenna arrays. The center-to-center distance of the discs is the same.

3. Results and discussions

We have performed both numerical simulations (FDTD module, Lumerical Inc.) and experimental measurements to characterize the performance of the flat lens.

Simulation results are shown in Fig. 2. Since there is no spatial variation of the antenna array in the y-direction, only one row of disc antennas was simulated and Bloch boundary conditions were applied in the y-direction. To monitor the phase profile created by the lens with an oblique incidence, a monitor was placed $2\lambda_0$ away from the lens surface to record data for the propagating waves only. Figure 2(a) shows the phase profile (phase of the E_y component for s-polarized incident light) at the monitor with a resolution of 0.1 μm. The fuzziness is mainly due to the incomplete phase coverage and the variation of the scattering amplitude of antennas (Appendix). The correlation coefficient of the curve fit is $R^2 = 0.99$, indicating a very good agreement between the designed phase profile and the ideal phase profile (black solid line) calculated from the design Eq. (1). The transmission data from the monitor, which can be calculated by the amplitude profile, is 84%, i.e. the amount of power transmitted through monitors, normalized to the source power. Figure 2(b) is the calculated distribution of the electric field intensity (normalized $|E|^2$) near the focal region in the x-z

Optics EXPRESS

plane. It was obtained by propagating the field data obtained from the near-field monitor to the far-field (see [24]). Figure 2(c) shows the reflected beam intensity (normalized $|E|^2$ in log scale) from the flat lens along a semicircle of radius 80 mm, equal to the focal length of the lens. Only a focused beam at θ = 0° is observed. We have verified this experimentally (see Appendix).

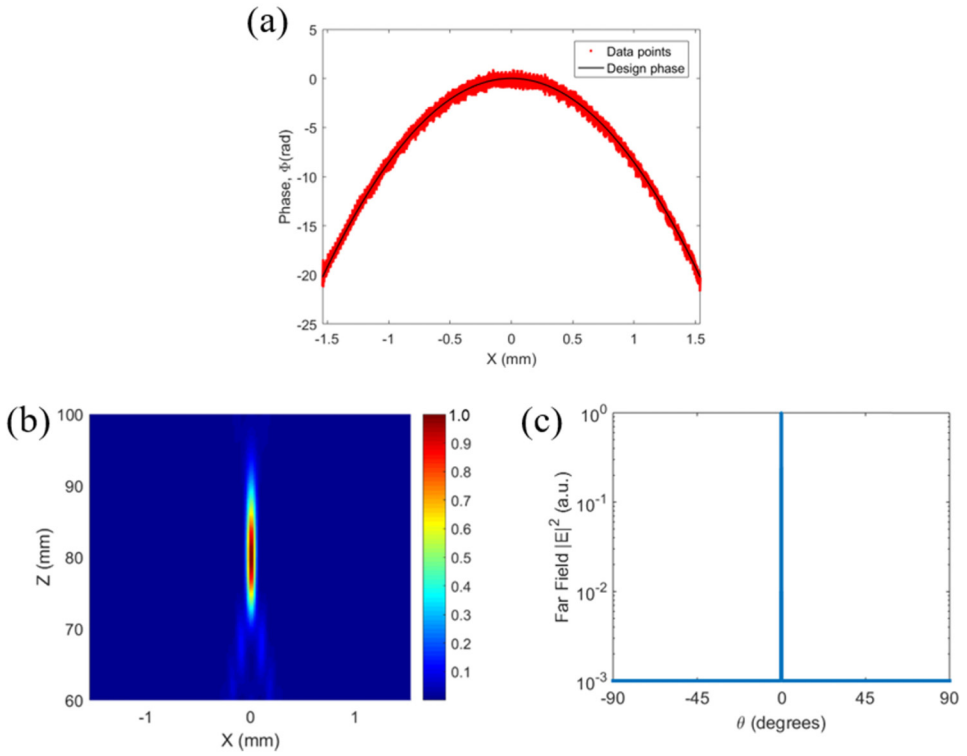

Fig. 2. FDTD simulation results of the flat lens. (a) Phase profile created by the lens weighted by the respective reflectance amplitude for an oblique incidence at θ = 45°. (b) Distribution of the intensity (normalized $|E|^2$) of the reflected beam in the x-z plane at y = 0. The lens is centered at x = 0 and the size of the lens is from –1.54 mm to 1.54 mm. (c) Far-field angular scan of the reflected beam with the scan radius equals to the focal length).

For the experimental characterization of the lens, we used a continuous-wave Fabry-Pérot quantum cascade laser (QCL) (AdTech Optics) emitting at λ = 4.6 μm. The laser was mounted so that its output beam is s-polarized (electric field along y-direction). We operated the laser near threshold so that the emitted beam is in a single mode. The full beam waist of the laser was 3 mm. The focusing beam created by the reflectarray was collected by a thermoelectrically-cooled mercury-cadmium-telluride detector (VIGO Systems) mounted on motorized rotation and translation stages. To increase the spatial resolution of the scans the light was first sent through a 30 μm pinhole before reaching the detector. The signal-to-noise ratio was increased by modulating the intensity of the QCL with a small sinusoidal current superimposed on the dc current (Wavelength Electronics QCL1500) and demodulating the detected signal with a lock-in amplifier (AMETEK Advanced Measurement Technology).

The reflected focused light from the flat lens was characterized experimentally by angular and translational scans as shown in Fig. 3(a) and 3(b), respectively. The data were taken at the center of the focal line, i.e. y = 0. The experimental results are in good agreement with the simulations. The average standard deviation of repeated measurements is 0.2%. Note that the step sizes used in scanning the reflected beam in Fig. 3(a) was 0.01° (equivalent to 14 μm in the x-direction) and in Fig. 3(b) was 10 μm, both smaller than the pinhole diameter (30 μm),

Optics EXPRESS

so the raw data are a convolution of the true signal and the pinhole response function. Hence, deconvolution was performed to retrieve the original beam profiles. Figure 3(a) shows that the measured reflection angle is 0°, which agreed well with the design equation. The full width at half maximum (FWHM) is less than 0.1°. Figure 3(b) shows that the full beam waist at $1/e^2$ of the peak intensity (indicated by the two black arrows) is 164 μm in the experiment and 166.5 μm in the simulation. The diffraction-limited full beam waist ($2w_0$) is 156 μm, calculated by Fourier transformation of an ideal continuous focusing phase profile. Our measured focused beam size is close to the diffraction limit. The difference is likely due to the incomplete phase coverage and the variation of the reflectance amplitude of the antennas (Appendix). Since our lens focuses light into a line, we checked the focused beam profile at other y positions and verified that the focus is near diffraction-limited along the focal line (see Appendix). It is worth pointing out that although the results shown are for s-polarized incident light, we have simulated and measured the lens with p-polarized incident light and found that $2w_0$ = 167 μm. Hence, the focusing performance of our lens is near polarization-independent (Appendix).

The measured focusing efficiency of the lens was η = 80% which is close to the simulated value of 83%. Most of the loss comes from the metal. Experimentally, the focused beam power was measured by placing a laser power meter (Nova, Ophir Photonics) in the focal region with an iris (~3 mm in diameter) in front to block non-focused light. Note that since the incidence angle was 45°, the effective incident beam size along the lens surface was bigger than the size of the lens, hence, the portion of the incident power on the lens was 82%, which was used to calculate the focusing efficiency. In the simulation, η was calculated by taking the ratio of the optical power in the focal region in Fig. 2(c) and the incident power. The discrepancy is likely due to fabrication errors. The reasons that enabled us to achieve high efficiency are: (1) reflectarray structures enable us to achieve a large phase coverage of 2π without the need of polarization conversion; (2) material (gold) used in our structure has a low loss in the mid-IR; (3) fabrication and experiment techniques: in [18], authors used a similar structure as ours (metal/dielectric/metal reflectarrays), but the highest efficiency demonstrated was 27% compared to 78% in simulation. It was mentioned in [18] that the discrepancy was due to the fabrication errors.

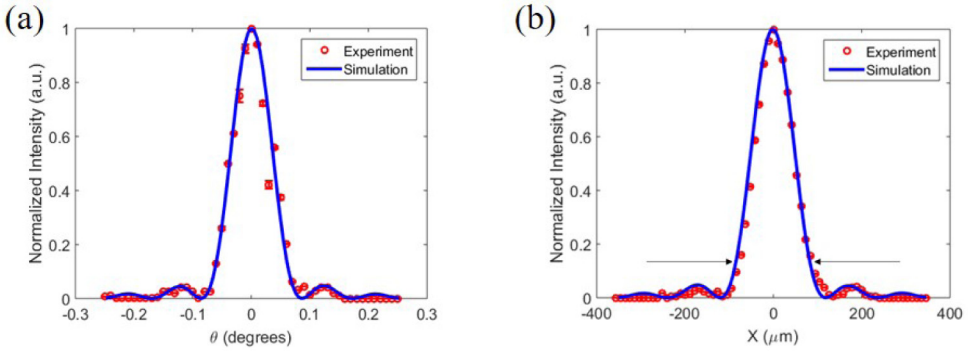

Fig. 3. Angular scan (a) and translational scan (b) of the reflected beam intensity (normalized $|E|^2$) measured at the center of the focal line. The arrows in (b) indicate the full beam waist measurement in μm.

4. Effects of incidence angle and wavelength

Table 1 shows the effects of change of incidence angle of the reflectarray lens. The wavelength is fixed at 4.6 μm. The sign of the angle is defined in Fig. 1(a). If the incidence angle increases (or decreases) from the design angle (45°), the reflected light shifts to more negative (or positive) angles from the normal to the lens surface. The physical origin is that any deviation from the designed incidence angle introduces an extra phase gradient on the

Optics EXPRESS

surface of the lens, which cannot be compensated by the phase profiles of the antennas. Therefore, scattered waves from each antenna will not arrive at the designed focal line in phase, resulting in a shift in the position of the focal line. The focal length and the full beam waist, however, remain relatively constant as the incidence angle changes within ± 15° from the design angle.

The beam profiles at the center of the focal line for various incidence angles in Table 1 obtained by FDTD simulations are plotted in Fig. 4(a). The inset shows the difference between each curve taking the one at θ = 45° as the baseline. The difference between the beam profiles is less than 8%. We have cross-checked the results with experiment for θ = 35° and 55°, which are shown in Fig. 4(b). The simulations and experiments agree well with each other.

Table 1. Effects of incidence angle on reflectarray lens (NA = 0.02) at λ_0 = 4.6 μm.

Incidence angle (°)	Reflection angle (°)	Focal length (mm)	Full beam waist (μm)
30	12	76	163
35	7.7	78	165
40	3.7	80	167
45	0	80	166.5
50	–3.4	79	165.5
55	–6.5	79	165.5
60	–9.2	78	164.5

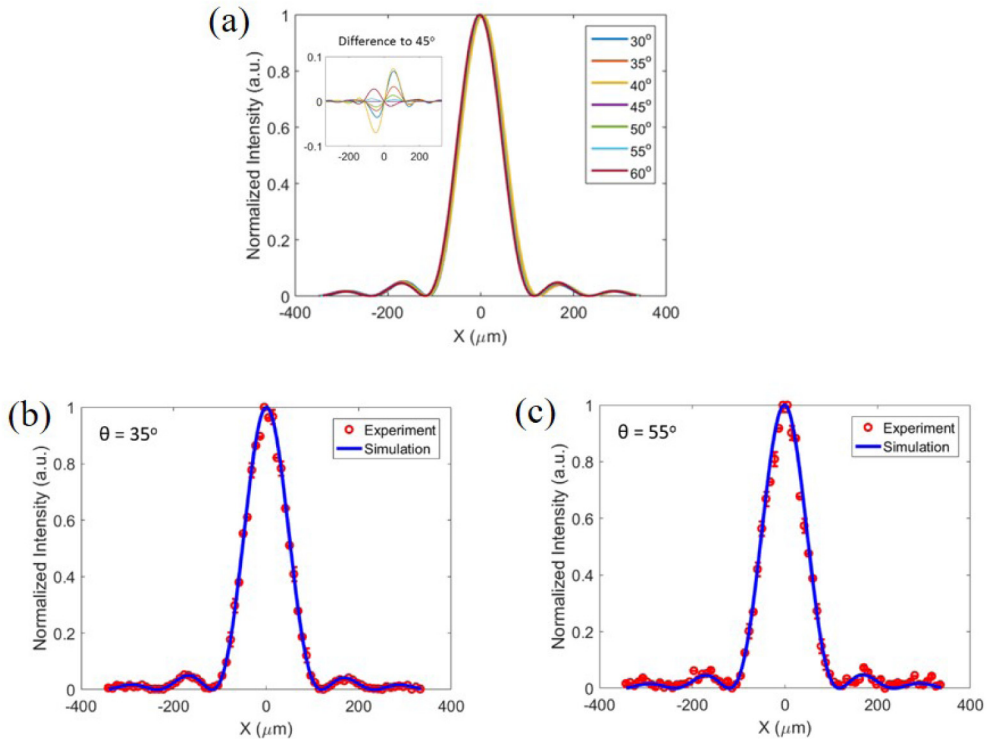

Fig. 4. (a) The focused beam profile for various incidence angles obtained by FDTD simulations. The inset shows the difference between the beam profiles and the one corresponding to an incidence angle of θ = 45°. Experimentally measured focused beam profiles for (b) θ = 35° and (c) θ = 55° compared with the simulation results.

Parabolic mirrors are widely used for focusing in the IR spectral range but are known to be very sensitive to the change of incidence angle [25]. Hence, we studied the effects of the

Optics EXPRESS

incidence angle of an off-axis parabolic mirror of the same NA using ray tracing techniques [25]. The result is shown in Table 2. The change in the reflection angle always equals the change in the incidence angle, which is expected for a mirror. But both the change in the reflection angle and the change in the focal length are larger than those of the reflectarrays as shown in Table 1. It is more clearly seen in the ray tracing plots of the reflectarray lens (red lines) and the parabolic mirror (blue lines) in Fig. 5(a)-5(c) where the incidence angle is 35°, 45°, and 55°, respectively. When θ = 45° (design angle), both the red and blue lines focus at x = 0 and z = f = 80 mm. When the incidence angle changes, the focus of the blue lines deviates more from the designed focus than that of the red lines. Hence, our reflectarray lens is not only thinner and lighter, but can also be designed to be less sensitive to the change in the incidence angle than a parabolic mirror in terms of reflection angle and focal length.

Table 2. Effects of incidence angle on parabolic mirror (NA = 0.02).

Incidence angle (°)	Reflection angle (°)	Focal length (mm)
30	15	86
35	10	85
40	5	83
45	0	80
50	–5	77
55	–10	73
60	–15	69

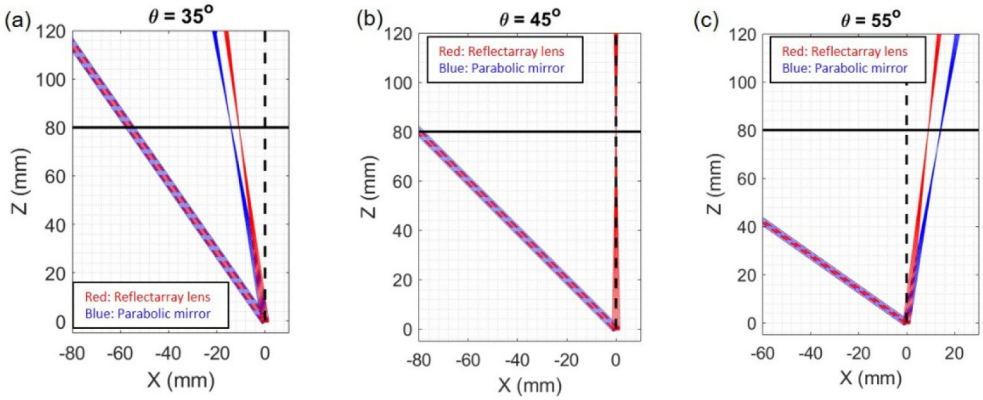

Fig. 5. Ray tracing plots of reflectarray lens and parabolic mirror of NA = 0.02 for incidence angles (a) θ = 35°, (b) θ = 45°, and (c) θ = 55°. The vertical black dashed line is at x = 0 and the horizontal black solid line is at z = 80 mm (focal length).

Studies of the effects of the incidence wavelength using FDTD simulations are summarized in Table 3. Depending on whether the incident wavelength is shorter or longer than λ_0 = 4.6 μm; the reflection angle is negative or positive, respectively. The focal length decreases but the full beam waist remains relatively constant as the incident wavelength increases.

Table 3. Effects of incidence wavelength on reflectarray lens for incidence angle θ = 45°.

λ (μm)	Reflection angle (°)	Focal length (mm)	Full beam waist (μm)
4	–5.3	91	165
4.6	0	80	166.5
5	3.6	73	167

5. Conclusions

In this paper, we designed a mid-IR flat lens that consists of a reflectarray of metallic antennas with subwavelength spacing. The focusing performance of the lens and effects of

Optics EXPRESS

incidence angle and wavelength were studied by experiments and simulations. We have achieved 80% focusing efficiency and near diffraction-limited focusing. One possible way to further improve the efficiency is to consider the optical impedance of the planar device to match with that of free space. Some of the examples are given in [6, 26, 27]. We found that the effects of incidence angle on the reflection angle and focal length were small for a deviation of the incidence angle within ± 15°, which compare favorably to an off-axis parabolic mirror with the same NA. Our approach based on illuminating the flat lens at an oblique angle has the advantage of a simplified experimental setup compared to other reflection-based measurements with normal incidence. Our lens has a number of attractive features, including high focusing efficiency, flexibility of design, polarization-independence, straightforward fabrication based on single-step photolithography, and reproducibility on a large scale.

Although our flat lens is not aberration-free, there are strategies to reduce coma [16, 28] and chromatic aberrations [29–34] of flat lenses. We envision that our flat lenses will complement or replace various conventional bulky optical components in systems for IR imaging, ranging, and detection, as well as for beam shaping of IR lasers and beacons.

6. Appendix

1. Phase response of antennas

We used FDTD simulations with periodic boundary conditions to find a set of phase shift elements with different radii that yielded both a large range of reflection phase and a relatively uniform reflection amplitude, as shown in Fig. 6. The unit cell configuration is shown in Fig. 1(b) in the main manuscript. The incident polarization is s-polarized. The phase coverage is from 0 to approximately 1.6π for discs with radii ranging from 0.4 μm to 1 μm. We note that the phase and reflectance are weakly dependent on the incidence angle, so we have tested two lens designs based on the phase response at the incidence angles of 0° and 45° and we found that the focusing performance is almost the same.

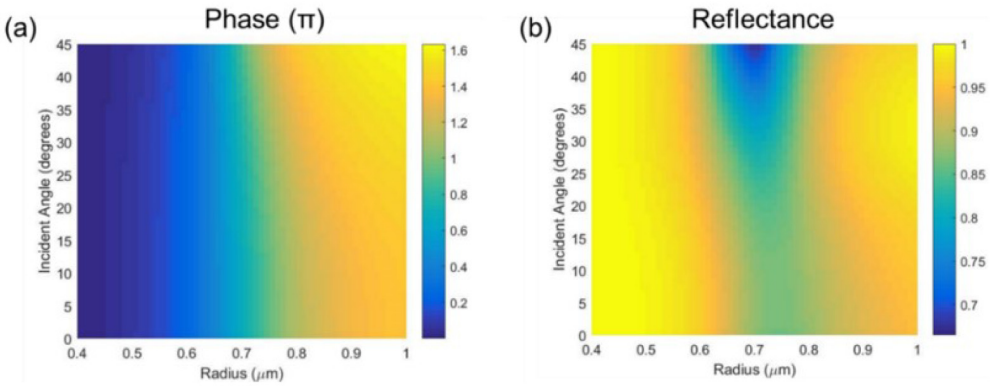

Fig. 6. (a) Phase and (b) amplitude response of antennas with varying disc radius for different incidence angles from 0° to 45°.

2. Reflected beams from the flat lens

Figure 7 shows the experimental results of an angular scan ranging from −50° to 10° with a step size of 1°. The range of the angular scan is limited by the experimental setup. In addition to the beam focused by the flat lens at θ = 0°, we also observed a reflected beam at θ = –45°. This is because the effective laser beam size along the lens surface was bigger than the lens; as a result, the portion of the light not incident on the lens was directly reflected by the gold

Optics EXPRESS

backplane. The intensity of the light at –45° is approximately 16.2% of the laser output power.

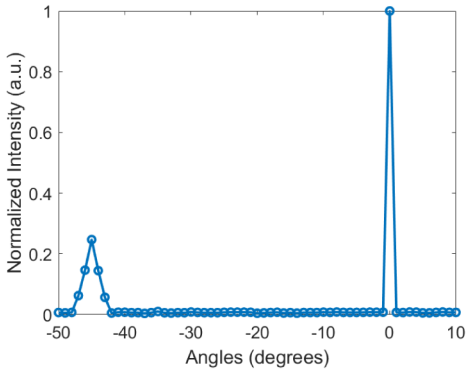

Fig. 7. Angular scan of the reflected beam intensity (normalized) from –50° to 10° at y = 0.

3. Characterization of the lens performance along the focal line

Since our lens is a cylindrical lens, the focus is a focal line. The data presented in the main manuscript were taken at y = 0. We expect that the focused beam profile does not change along the y-direction. We experimentally verified it at two other y positions, which are shown in Fig. 8(a) and 8(b). The full beam waist size is 166 μm and 165 μm at y = –0.75 mm and y = 1.4 mm, respectively. Recall that the full beam waist at y = 0 is 164 μm. The difference is small, so we conclude that there is no aberration along the focal line. However, we note that the focused beam intensity varies along the focal line as shown in Fig. 8(c). This is due to the intensity variation of the Gaussian beam source. The intensity drops to nearly zero beyond the size of the lens, i.e. –1.54 mm to 1.54 mm.

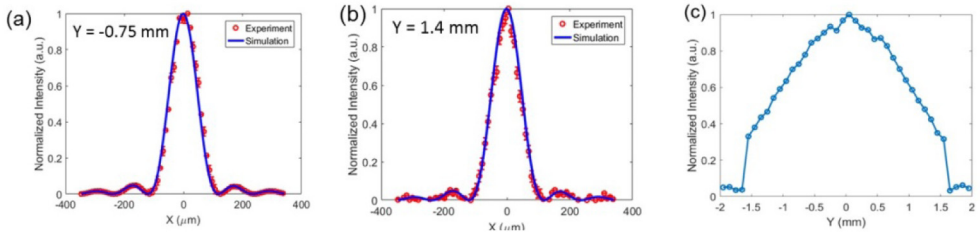

Fig. 8. Normalized focused beam profile at (a) y = –0.75 mm and (b) y = 1.4 mm. (c) Normalized focused beam intensity as a function of y measured at x = 0. The step size of the measurement is 100 μm.

4. Focusing performance of p-polarized light

This section summarizes the simulation and measurement results when the incident light is p-polarized (electric field in the plane of incidence) with an incidence angle of θ = 45°. Experimentally, this was realized by mounting the QCL vertically. All measurements were performed on the same lens as in the main manuscript. We found that the focusing performance including the focal length, the beam waist at the focus, and the focusing efficiency is similar to that of the s-polarized light.

Figure 9 shows the FDTD simulations of the flat lens with p-polarized illumination. Figure 9(a) is the distribution of the electric field intensity (normalized |E|2) around the focal region in the x-z plane. The focal length is 80 mm. Figure 9(b) shows the reflected beam intensity (normalized $|E|^2$ in log scale) along with a semicircle of radius of 80 mm. The

Optics EXPRESS

focusing efficiency is 82% (simulation) and 78% (experiment), which is slightly lower than that of the s-polarized light.

The reflected focused light from the flat lens was characterized experimentally by angular and translational scans as shown in Fig. 9(c) and 9(d), respectively. The experimental results are in good agreement with the simulations. The scanning parameters are the same as that for the s-polarized light and deconvolution was performed. The reflected light was focused at 0° and the full beam waist ($2w_0$) at the focus was found to be 167 μm, both in the experiment and in the simulation.

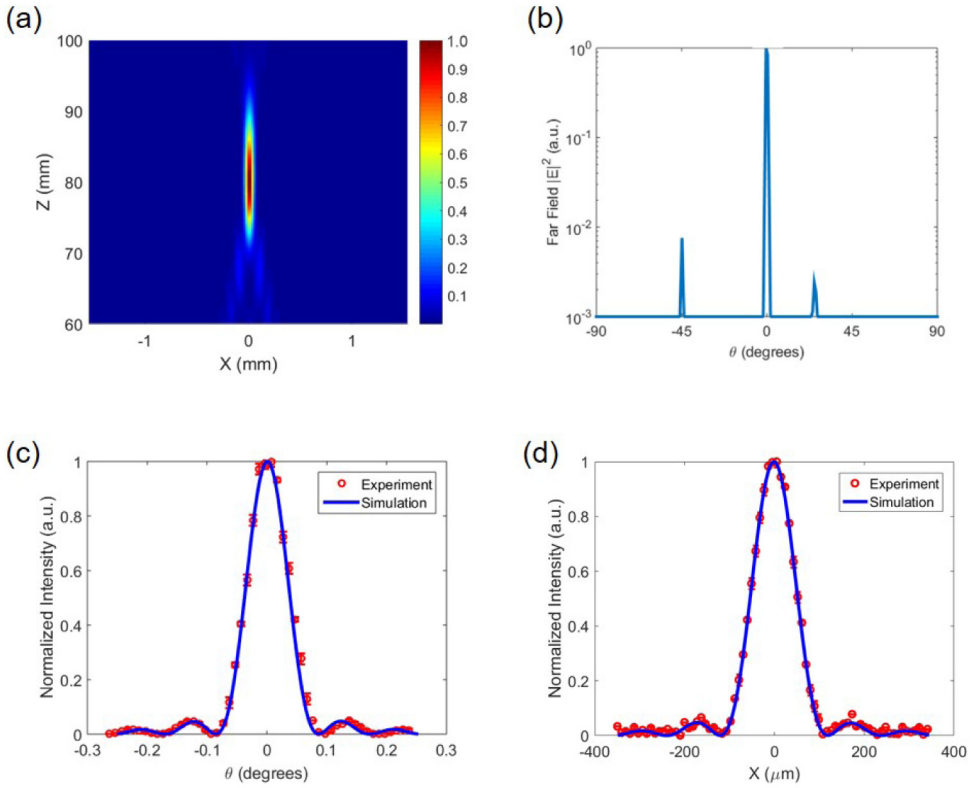

Fig. 9. Simulation and experimental results of the flat lens with p-polarized incident light. (a) Distribution of the intensity (normalized $|E|^2$) of the reflected beam in the x-z plane. The antenna arrays are centered at x = 0. (b) Far-field projection of the reflected beam intensity (normalized $|E|^2$ in log scale) showing that the majority of the light was focused at 0° (normal to the lens surface). (c) Angular scan and (d) Translational scan of the reflected beam intensity (normalized $|E|^2$) at the focus.

Funding

Air Force Office of Scientific Research (AFOSR) (MURI: FA9550-12-1-0389); National Science Foundation (ECCS-1307948, 1541959); and Charles Stark Draper Laboratory (SC001-0000000731); National Science Scholarship from A*STAR, Singapore.

Acknowledgments

We acknowledge Mikhail A. Kats and Steven Byrnes for helpful discussions and Elodie Strupiechonski for the valuable advice on the experiments. This work was performed in part at the Center for Nanoscale Systems (CNS), a member of the National Nanotechnology Coordinated Infrastructure (NNCI), which is supported by the National Science Foundation. CNS is part of Harvard University.